Arch. Mech., **60**, 6, pp. 491–507, Warszawa 2008
SIXTY YEARS OF THE ARCHIVES OF MECHANICS

Third-order method for simulation of compressible flows[*)]

R. WIETESKA[†], J. ROKICKI

Warsaw University of Technology
Institute of Aeronautics and Applied Mechanics
Nowowiejska 24, 00-665 Warsaw, Poland
e-mail: jack@meil.pw.edu.pl

THE PAPER DISCUSSES finite volume WENO reconstruction applied to simulation of compressible 3D Euler flows. The main objective of this work is presentation of the new reconstruction procedure (third-order of accuracy in space), together with the procedure for integration of numerical fluxes applied to simulations of compressible 3D Euler flows, using unstructured meshes.

1. Introduction

SIMULATION OF compressible flows with shockwaves is still an important area of research with significant impact on industrial applications. In 3D cases and on unstructured meshes numerical viscosity has a significant adverse effect on accuracy, especially when prediction of the drag coefficient is considered.

Traditionally, in CFD second-order accurate numerical methods are preferred in practical calculations. Those methods are characterised by simplicity and robustness, but large amount of spurious entropy production leads to problems with drag coefficient calculations. High-order methods are often perceived as less robust as well as very difficult to implement on unstructured meshes.

The aim of this paper is a detailed investigation of the new (third-order) finite volume discretisation used for simulation of 3D compressible flows on unstructured meshes.

2. Finite Volume Method

2.1. Euler model

In present work the Euler model of the fluid is used. The equations of state in conservative form can be expressed as:

[*)]The paper was presented at XVIII Polish Conference of Fluid Mechanics (KKMP), Jastrzębia Góra, 21–25 September, 2008.

[†)]Robert Wieteska died on 30 October, during the publication process of this paper.

$$\frac{\partial \mathbf{U}}{\partial t} + \nabla \cdot \mathcal{F}(\mathbf{U}) = 0, \tag{2.1}$$

$$\mathbf{U} = \begin{bmatrix} \rho \\ \mathbf{m} \\ \varepsilon \end{bmatrix}, \qquad \mathcal{F}(\mathbf{U}) = \begin{bmatrix} \mathbf{m}^T \\ \frac{1}{\rho}\,\mathbf{m} \otimes \mathbf{m} + p\,\mathbf{I} \\ H\mathbf{m}^T \end{bmatrix}. \tag{2.2}$$

where in Eq. (2.2) ρ denotes density, $\mathbf{m} = \rho\mathbf{v}$ momentum vector, p pressure, ε total energy per unit volume, γ ratio of the specific heat capacities and H is the total enthalpy equal to:

$$H = \frac{\gamma\varepsilon}{\rho} - (\gamma - 1)\,\frac{\mathbf{m}^T\mathbf{m}}{2\rho^2}.$$

This system of equations has to be completed with the equation of state for perfect gas

$$p = (\gamma - 1)\left(\varepsilon - \frac{\mathbf{m}^T\mathbf{m}}{2\rho}\right). \tag{2.3}$$

2.2. Finite Volume Method discretization

Finite Volume Method consists in integration of the Euler equations over the control volume Ω_j. After integration one obtains:

$$\int\limits_{\Omega_j} \frac{\partial \mathbf{U}}{\partial t}\, d\Omega = -\int\limits_{\partial\Omega_j} \mathcal{F}(\mathbf{U})\,\mathbf{n}\,\partial\Omega_j. \tag{2.4}$$

Taking further $\overline{\mathbf{U}}_j$ as the cell average value of $\mathbf{U}$ in the volume Ω_j:

$$\overline{\mathbf{U}}_j = \frac{1}{|\Omega_j|}\int\limits_{\Omega_j} \mathbf{U}\, d\Omega, \qquad |\Omega_j| = \mathrm{Vol}(\Omega_j), \tag{2.5}$$

the above relation can be rewritten as:

$$\frac{d}{dt}\overline{\mathbf{U}}_j = -\frac{1}{|\Omega_j|}\int\limits_{\partial\Omega_j} \mathcal{F}(\mathbf{U})\cdot\mathbf{n}\, ds. \tag{2.6}$$

Because the typical grids used in the calculations consist of simple shapes (triangles, quadrilaterals, tetrahedrals), we can rewrite the right-hand side of the Eq. (2.6) in the much more simple form as:

$$\int\limits_{\partial\Omega_j} \mathcal{F}(\mathbf{U})\cdot\mathbf{n}\, ds \;=\; \sum_i \int\limits_{\Gamma_i} \mathcal{F}(\mathbf{U})\cdot\mathbf{n}_i\, ds = \sum_i \mathcal{F}_i^{\star}(\mathbf{U}), \tag{2.7}$$

$$\mathcal{F}_i^{\star}(\mathbf{U}) \stackrel{\mathrm{def}}{=} \int\limits_{\Gamma_i} \mathcal{F}(\mathbf{U})\cdot\mathbf{n}_i\, ds, \tag{2.8}$$

where $\mathcal{F}_i^\star(\mathbf{U})$ is a numerical flux which must be calculated using $\mathbf{U}$ at each cell face rather than taking the average value from the cell center. This numerical flux is calculated by the usual procedure of solving the simplified Riemann problem. Finally the Finite Volume discretisation of the Euler equation can be expressed as

$$\frac{d}{dt}\overline{\mathbf{U}}_j = -\frac{1}{|\Omega_j|}\sum_i \mathcal{F}_i^\star(\mathbf{U})\,. \tag{2.9}$$

Collection of Eqs. (2.9) written for all control volumes forms a system of nonlinear differential equations. In the present paper only a stationary case is considered. In the present version, the control volumes coincide with mesh cells while unknowns are assigned to cell's centre (cell-centered approach).

3. Third-order reconstruction

In order to calculate fluxes at the cell walls, the solution is reconstructed within each cell using the information from the neighbouring cells. The order of spatial discretisation depends on two factors:

- the order of reconstruction within the cell,
- the order of integration formula used at the cell walls to calculate the fluxes.

The next subsections are devoted to the new third-order reconstruction procedure and the integration method. This approach is subsequently coupled with the WENO (Weighted Essentially Non-Oscillatory) method to eliminate non-physical oscillations in the numerical process.

3.1. Gradient calculation – indirect method

In the first approach which generalises the ideas of SHU [1], the higher-order gradient is calculated using linear combination of 1-st order accurate gradients calculated on different local stencils. We shall assume now that φ_p denotes function value at the p-th cell ($p = 0$ corresponds to the cell in which gradient is reconstructed).

3.1.1. First step. The Taylor expansion formula can be written as:

$$\varphi_p - \varphi_0 = \mathbf{r}_{p0}^T \cdot \nabla\varphi\Big|_0 + \frac{1}{2}\mathbf{r}_{p0}^T \cdot \nabla^2\varphi\Big|_0 \mathbf{r}_{p0} + O\left(h^3\right), \tag{3.1}$$

where $\mathbf{r}_{p0} = \mathbf{r}_p - \mathbf{r}_0$ denotes distance between the respective cell centres (see Fig. 1), while $\nabla^2\varphi = \left[\partial^2\varphi/\partial x_i \partial x_j\right]$ is the Hessian matrix (h denotes the characteristic size of the cell).

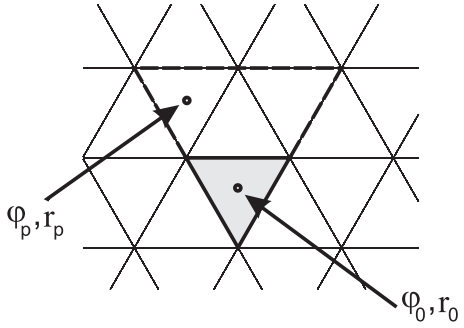

FIG. 1. Typical stencil used for indirect method (r_0, r_p denote the positions of the corresponding cell centers, φ is the function value).

The gradient can be approximated as a linear combination of function increments:

$$\mathbb{G}\boldsymbol{\varphi} = \sum_{p=1}^{m} \mathbf{G}_p \cdot w_p \cdot (\varphi_p - \varphi_0)\,, \tag{3.2}$$

where w_p are the known linear weights. Usually w_p is taken proportional to

$$w_p = \frac{1}{\|\mathbf{r}_{p0}\|}.$$

The problem consists in finding such coefficients $\mathbf{G}_p$, which depend only on the local geometry of the mesh. For tetrahedral cells $m = 4$, for triangles $m = 3$ (Fig. 1). After substituting (3.2) into (3.1) one obtains:

$$\mathbb{G}\boldsymbol{\varphi} = \sum_{p=1}^{m} \mathbf{G}_p w_p \left[\mathbf{r}_{p0}^T \nabla\varphi\Big|_0 + \frac{1}{2}\mathbf{r}_{p0}^T \nabla^2\varphi\Big|_0 \mathbf{r}_{p0} + O\left(h^3\right)\right],$$

$$\mathbb{G}\boldsymbol{\varphi} = \sum_{p=1}^{m} \mathbf{G}_p w_p \mathbf{r}_{p0}^T \nabla\varphi\Big|_0 + \frac{1}{2}\sum_{p=1}^{m} \mathbf{G}_p w_p \mathbf{r}_{p0}^T \nabla^2\varphi\Big|_0 \mathbf{r}_{p0} + O\left(h^2\right). \tag{3.3}$$

In order to obtain the first-order formula:

$$\mathbb{G}\boldsymbol{\varphi} = \nabla\varphi\Big|_0 + O\left(h\right) \tag{3.4}$$

one should compare Eqs. (3.4) and (3.3):

$$\nabla\varphi\Big|_0 + O\left(h\right) = \sum_{p=1}^{m} \mathbf{G}_p w_p \mathbf{r}_{p0}^T \nabla\varphi\Big|_0 + \frac{1}{2}\sum_{p=1}^{m} \mathbf{G}_p w_p \mathbf{r}_{p0}^T \nabla^2\varphi\Big|_0 \mathbf{r}_{p0} + O\left(h^2\right), \tag{3.5}$$

which produces the system of linear equations with the unknown coefficients $\mathbf{G}_p$:

$$\sum_{p=1}^{m} \mathbf{G}_p w_p \mathbf{r}_{p0}^T = \mathbf{I}. \tag{3.6}$$

This system is under/over–determined and is solved in the least-square sense by applying a sequence of Householder transformations. In different form this system can be expressed as:

$$\forall \mathbf{e} \in \mathbb{R}^n, \qquad \sum_{p=1}^{m} \mathbf{G}_p w_p \mathbf{r}_{p0}^T \mathbf{e} = \mathbf{e}. \tag{3.7}$$

3.1.2. Second step. To increase the order of the method a collection of stencils around the cell is used. The known coefficients $\mathbf{G}_{p\alpha}$ $(\alpha = 1, \ldots, m')$ for each stencil are used for calculation of a gradient with second-order accuracy. A collection of stencils used in calculations (for 2D case) is presented in Fig. 2.

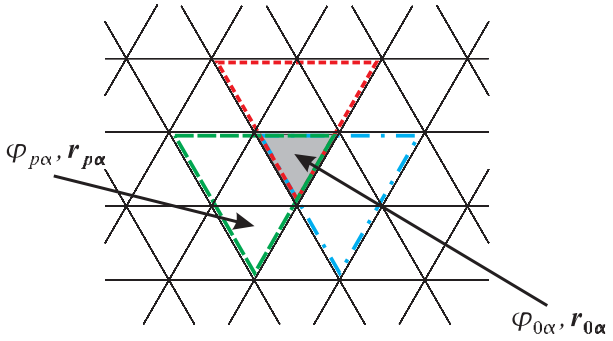

FIG. 2. Collection of stencils used in the indirect method (α – denotes stencil number, p – denotes local cell number).

On each stencil α the first-order gradient can be expressed now as:

$$\begin{aligned} \mathbb{G}^{\alpha}\boldsymbol{\varphi} &= \nabla\varphi\Big|_0 + \frac{1}{2}\sum_{p=1}^{m} \mathbf{G}_{p\alpha} w_{p\alpha} \mathbf{r}_{p0\alpha}^T \cdot \nabla^2\varphi\Big|_0 \mathbf{r}_{p0\alpha} + O\left(h^2\right), \\ \mathbf{r}_{p0\alpha} &= \mathbf{r}_{p\alpha} - \mathbf{r}_{0\alpha}, \end{aligned} \tag{3.8}$$

On the other hand on each stencil α

$$\mathbb{G}^{\alpha}\boldsymbol{\varphi} = \sum_{p=1}^{m} \mathbf{G}_{p\alpha} \cdot w_{p\alpha} \cdot (\varphi_{p\alpha} - \varphi_{0\alpha}). \tag{3.9}$$

Higher-order gradient can be obtained by linear combination of lower-order gradients.

$$\mathbb{G}\boldsymbol{\varphi} = \sum_{\alpha=0}^{m'} \mathbf{M}_{\alpha} \cdot \mathbb{G}^{\alpha}\boldsymbol{\varphi} + O\left(h^2\right). \tag{3.10}$$

Comparing Eqs. (3.10) and (3.8) where $\mathbf{M}_\alpha$ are unknown matrix coefficients, one obtains

$$\nabla\varphi\Big|_0 = \left(\sum_\alpha \mathbf{M}_\alpha\right)\nabla\varphi\Big|_0 + \frac{1}{2}\sum_\alpha \mathbf{M}_\alpha \sum_{p=1}^{m} \mathbf{G}_{p\alpha} w_{p\alpha} \mathbf{r}_{po\alpha}^T \nabla^2\varphi\Big|_0 \mathbf{r}_{p0\alpha}. \tag{3.11}$$

The second-order approximation requires one to solve (in a least square sense) an under/over–determined linear systems for unknown matrices $\mathbf{M}_\alpha$:

$$\begin{aligned} &\sum_\alpha^{m'} \mathbf{M}_\alpha = \mathbf{I} \qquad \left(\mathbf{M}_\alpha = \mathbf{M}_\alpha^T\right), \\ &\forall\ \mathbf{E} \equiv \mathbf{E}^T \in \mathbb{R}^{3\times 3}, \qquad \sum_\alpha^{m'} \mathbf{M}_\alpha \sum_{p=1}^{m} \mathbf{G}_{p\alpha} w_{p\alpha} \mathbf{r}_{p0\alpha}^T \mathbf{E} \mathbf{r}_{p0\alpha} = \mathbf{0} \end{aligned} \tag{3.12}$$

(m' denotes the number of stencils).

3.2. Gradient calculation – direct method

Analogous procedure as that presented in the previous subsection was adopted for the direct method to calculate a gradient with the second-order accuracy. The starting point is also a Taylor expansion formula

$$\varphi_p - \varphi_0 = \mathbf{r}_{p0}^T \cdot \nabla\varphi\Big|_0 + \frac{1}{2} \cdot \mathbf{r}_{p0}^T \nabla^2\varphi\Big|_0 \mathbf{r}_{p0} + O(h^3)$$

but unlike in the previous subsection, we construct a larger stencil containing more cells (for a 2D case see Fig. 3).

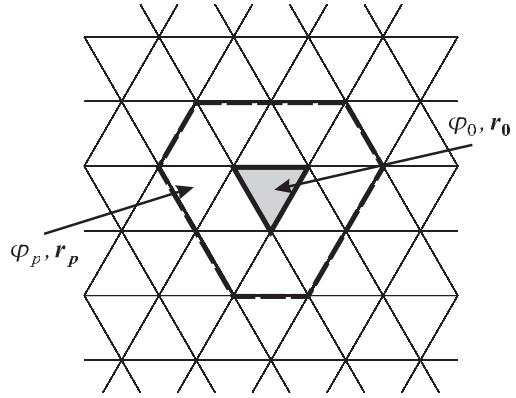

FIG. 3. Typical stencil used for the direct method.

Again the gradient $\mathbb{G}\boldsymbol{\varphi}$ is expressed as in Eq. (3.2), but in this variant the gradient has to be calculated directly with the second-order accuracy:

$$\mathbb{G}\boldsymbol{\varphi} = \nabla\varphi|_0 + O\left(h^2\right). \tag{3.13}$$

Substituting incremental form of the gradient (3.2) into the Taylor formula and reordering terms, one obtains:

$$\mathbb{G}\boldsymbol{\varphi} = \sum_{p=1}^{m} \mathbf{G}_p w_p \mathbf{r}_{p0}^T \nabla\varphi\Big|_0 + \frac{1}{2}\sum_{p=1}^{m} \mathbf{G}_p w_p \mathbf{r}_{p0}^T \nabla^2\varphi\Big|_0 \mathbf{r}_{p0} + O\left(h^2\right)$$

and finally the expression that helps to find the unknown coefficients:

$$\nabla\varphi\Big|_0 + O\left(h^2\right) = \sum_{p=1}^{m} \mathbf{G}_p w_p \mathbf{r}_{p0}^T \nabla\varphi\Big|_0 + \frac{1}{2}\sum_{p=1}^{m} \mathbf{G}_p w_p \mathbf{r}_{p0}^T \nabla^2\varphi\Big|_0 \mathbf{r}_{p0} + O\left(h^2\right).$$

In this case it is needed to solve the linear system in the form:

$$\begin{aligned} &\forall\ \mathbf{e} \in \mathbb{R}^3, && \sum_{p=1}^{m} \mathbf{G}_p w_p \mathbf{r}_{p0}^T \mathbf{e} = \mathbf{e}, \\ &\forall\ \mathbf{E} \equiv \mathbf{E}^T \in \mathbb{R}^{3\times 3}, && \sum_{p=1}^{m} \mathbf{G}_p w_p \mathbf{r}_{p0}^T \mathbf{E}\mathbf{r}_{p0} = \mathbf{0}. \end{aligned} \tag{3.14}$$

Restriction for symmetry of $\mathbf{E}$ corresponds to the symmetry of the Hessian. In this variant the number of equations is equal to $n + n\,(n+1)\,/2$, the number of unknowns is $m \cdot n$ (n is a space dimension, m is a number of cells in stencil and may be different for different stencils in the grid). Minimal $m = 9$ in $\mathbb{R}^3$ is needed, but for the typical grids this case hardly ever appears (is eliminated during the triangulation process). For the typical grid in 3D the number of cells that create such stencil is usually equal to $50 \div 60$. It is important to note that the cost of the indirect method is much higher than the present direct method [6]. Therefore the direct method will be used further in numerical experiments.

3.3. Hessian calculation

A similar approach can be applied again to evaluate the Hessian:

$$\mathbb{H}\boldsymbol{\varphi} = \sum_{p=1}^{m} \mathbf{H}_p \cdot \tilde{w_p} \cdot (\varphi_p - \varphi_0) \tag{3.15}$$

where the weights $\tilde{w_p}$ can be assumed as $\tilde{w_p} = \left(1/\|\mathbf{r}_{p0}\|\right)^2$ and the $\mathbf{H}_p$ are unknown matrix coefficients. These coefficients can be found by solving the system:

$$
\begin{aligned}
&\forall\ \mathbf{e} \in \mathbb{R}^3, && \sum_{p=1}^{m} \mathbf{H}_p \tilde{w_p} \mathbf{r}_{p0}^T \mathbf{e} = \mathbf{0}, \\
&\forall\ \mathbf{E} \equiv \mathbf{E}^T \in \mathbb{R}^{3\times 3}, && \sum_{p=1}^{m} \mathbf{H}_p \tilde{w_p} \mathbf{r}_{p0}^T \mathbf{E} \mathbf{r}_{p0} = \mathbf{E}.
\end{aligned} \tag{3.16}
$$

3.4. Numerical integration

All numerical schemes adopted for FVM require numerical integration of fluxes on the cell walls [4]. In the present work, a Gauss–Legendre quadrature method for numerical integration over the standard triangular surface was adopted. $\mathcal{F}_i^\star(\mathbf{U})$ (see Eq. (2.9)) is obtained as a sum of partial fluxes calculated in the specific point (see Fig. 4) defined as

$$
\mathbf{r}^j = \mathbf{r}_c + \frac{1}{2}\mathbf{r}_{jc}, \qquad j = 1, 2, 3, \tag{3.17}
$$

where $\mathbf{r}_c$ is a geometrical center of the wall while $\mathbf{r}_{jc}$ connects the wall center with the wall vertex.

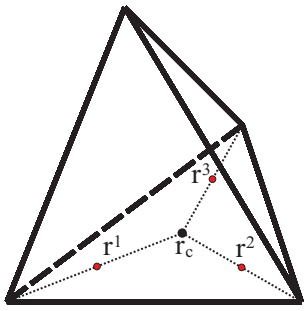

FIG. 4. Gaussian quadrature points used for integration over the triangle.

All quadrature weights are equal to 1/3. Finally, the numerical flux for a typical wall can be expressed as:

$$
\mathcal{F}_i^\star(\mathbf{U}) = \frac{1}{3}\sum_{j=1}^{3} \mathcal{F}_i^j(\mathbf{U}). \tag{3.18}
$$

4. Nonlinear weighting

The reconstruction proposed in Sec. 3 is linear in nature. Therefore it cannot lead to monotonicity in the vicinity of discontinuities (Godunov theorem). Two approaches can be used to suppress unphysical oscillations:

- nonlinear weighting between different high-order reconstructions (WENO – Weighted Essentially Non-Oscillatory type approach [1–3]);
- lowering the order of reconstruction near discontinuities (MUSCLE-type approach [5]).

Both approaches were implemented and compared. In both cases several stencils $S_1, S_2, S_3, \ldots, S_M$ were used for each control volume Ω_h (see Fig. 5). In both cases the central stencil S_1 was built by collecting cells having at least one vertex in common with the Ω_h cell (see solid-line polygon in Fig. 5). This is in contrast to the second-order procedure in which stencil consists of cells which have exactly one wall in common with Ω_h. For the WENO case additional biased stencils were added, each biased stencil being in fact central stencil for the cell which has a common wall with Ω_h (cells with light dots in their centre in Fig. 5). This algorithm to select stencils is completely general and fully applicable to 2D and 3D general meshes.

The WENO- type approach consists of the following steps:

- Obtain a third-order reconstruction polynomial, denoted by p_i, associated with each stencil S_i, which approximates the solution on Ω_h.
- Calculate oscillation indicator o_i for each function p_i.
- Calculate weights for each p_i using oscillation indicator o_i.
- Find the global reconstruction function for a control volume Ω_h as a weighted average of all p_i.

The MUSCLE-type approach consists of the following steps:

- Obtain a lower-order gradient $\mathbb{G}_I$ and the second-order gradient $\mathbb{G}$ (using direct procedure).

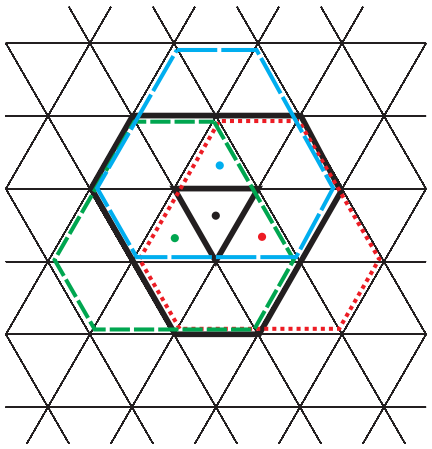

FIG. 5. A series of stencils used in the third-order WENO reconstruction procedure (solid line triangle – the Ω_h cell, solid line polygon – central stencil, broken line polygons – biased stencils).

- For the smooth fields, $\mathbb{G}_I$ and $\mathbb{G}$ should differ by the first-order term:

$$\|\mathbb{G}_I - \mathbb{G}\|_2 \sim \mathcal{C}_\star \cdot h, \tag{4.1}$$

where h is the local cell size, while the constant $\mathcal{C}_\star$ is related to the norm of the Hessian. The ratio:

$$\mathcal{C}_\star = \frac{\|\mathbb{G}_I - \mathbb{G}\|_2}{h} \tag{4.2}$$

is therefore used to design a continuous switching function allowing to reduce the approximation order in the neighbourhood of discontinuity. It is assumed that $\mathcal{C}_\star < \mathcal{C}_{\max}$ corresponds to the smooth field where the third-order reconstruction is possible. Therefore, modified gradient $\widehat{\mathbb{G}}$ and Hessian $\widehat{\mathbb{H}}$ are calculated as:

$$\widehat{\mathbb{G}} = \theta \cdot \mathbb{G} + (1-\theta) \cdot \mathbb{G}_I, \qquad \widehat{\mathbb{H}} = \theta \cdot \mathbb{H} \tag{4.3}$$

where:

$$\theta = \exp(-\max(0, \mathcal{C}_\star - \mathcal{C}_{\max})^4) \tag{4.4}$$

and the value of $\mathcal{C}_{\max}$ is taken equal to 10.

Numerical experiments show that the results obtained by WENO scheme are significantly better, especially for fully transonic flows. In the MUSCLE-type approach (as it is shown in Fig. 6) the residual error is stabilized prior to achieving convergence (even if the value of $\mathcal{C}_{\max}$ is changed).

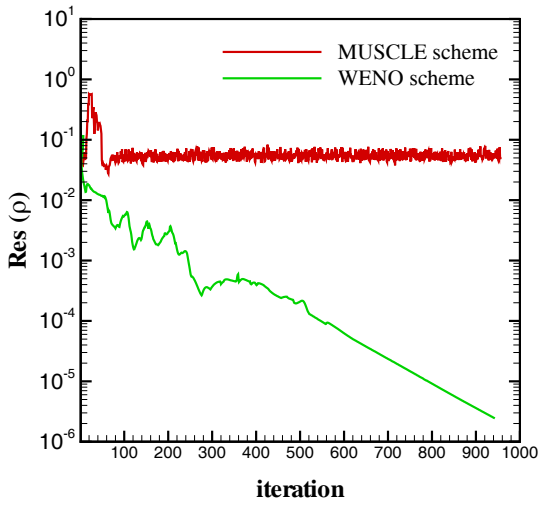

FIG. 6. Comparison of convergence for WENO and MUSCLE-type schemes.

4.1. The WENO reconstruction

In our case the reconstructed function for each control volume is given with the third-order accuracy on each stencil $S_1, \ldots, S_M$. The final WENO reconstruction for each control volume is defined as a weighted average

$$p_h = \sum_{i=1}^{M} \omega_i \cdot p_i. \tag{4.5}$$

Oscillation indicator can be defined as:

$$o_i = \sum_{1 \le |\alpha| \le \zeta} \int h^{2|\alpha|-1} \left\| D^\alpha p_i(x) \right\|^2 d\Omega, \tag{4.6}$$

where ζ is an order of accuracy, h a typical linear size of the cell and M is a number of stencils used for the local reconstruction (α denoting a multiindex[*)]).

The weights are calculated using algebraic formula:

$$\omega_i = \frac{(\varepsilon + o_i)^{-r}}{\sum_{i=1}^{M} (\varepsilon + o_i)^{-r}}. \tag{4.7}$$

In the above, parameter r determines the behaviour of the scheme ($r = 4$ [3]). Increasing r results in increasing the influence of a single stencil. In the limit $r \to \infty$ formula (4.7) leads to ENO scheme where only one stencil out of many is used for reconstruction. Following [3] the additional parameter ε is chosen to be around 10^{-6}. Its role is to eliminate problems in areas where o_i approaches zero (e.g., near stagnation points).

5. Numerical tests

5.1. Sinusoidal bump

The performance of the full method was investigated for the compressible flow in the 3D channel with sinusoidal bump. The height, width and the length of the channel were 0.5, 0.4 and 2.0 respectively. The shape of the lower wall was described by the function

$$z_L(x) = \begin{cases} 0 & x \notin \langle 0, 1 \rangle, \\ \frac{1}{2} \sin^2(\pi x) & x \in \langle 0, 1 \rangle. \end{cases}$$

[*)] Because the reconstruction is of third-order of accuracy, $|\alpha| = 1, 2$ $(j, k = 1, 2, 3)$

$$D^{|\alpha|=1} = \frac{\partial}{\partial x_j}, \qquad D^{|\alpha|=2} = \frac{\partial}{\partial x_j} \frac{\partial}{\partial x_k}.$$

Nine meshes were generated. Number of cells in each grid and the characteristic cell size can be found in Table 1. Between consecutive meshes the cell size was changed (on average) as:

$$q = \frac{h_{k+1}}{h_k} = 2^{-2/9} \approx 0.85. \tag{5.1}$$

Figure 7 shows the typical grid used for the grid convergence studies.

Table 1. Grid parameters for the sinusoidal channel test.

k	characteristic size h_k	number of cells N_k
0	0.10000	2781
1	0.08524	4596
2	0.07349	7214
3	0.06300	11795
4	0.05400	18439
5	0.04629	28512
6	0.03968	47077
7	0.03403	73695
8	0.02916	116971

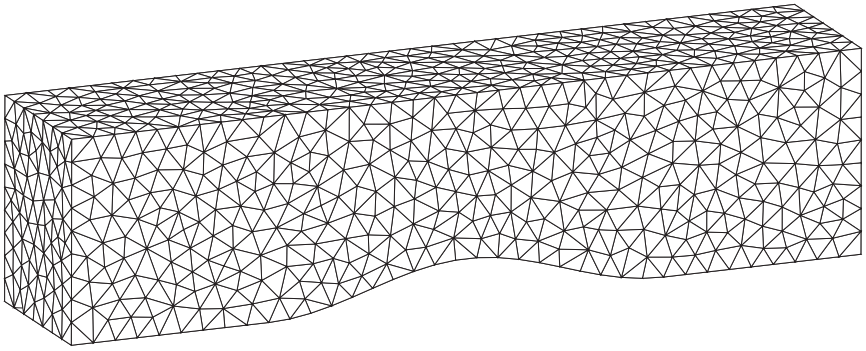

FIG. 7. Typical grid used for the sinusoidal channel test.

5.1.1. Subsonic test. The first comparison between the 2nd order WENO and the present 3rd order method for complete Euler algorithm was performed for the fully subsonic case (Ma = 0.5 at the inlet). Figure 8 shows the estimated error as a function of the stepsize h (the methodology to estimate the error was first introduced in [7] and subsequently generalised in [6]).

It is well visible that the new reconstruction procedure gives better (considering the slope of the line) results in comparison with the standard second-order method where only the gradient is calculated. Both approaches (direct and indirect – see Sects. 3.2 and 3.1) to calculate gradient provide similar accuracy.

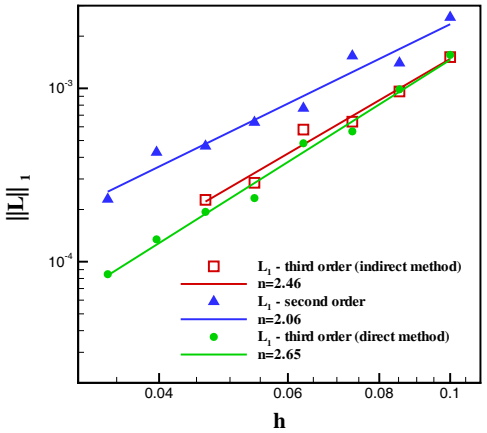

FIG. 8. Estimated $\|L\|_1$ error for subsonic flow in the channel.

Additionally it was shown in [6] that the method is not sensitive to significant deformation of the mesh cells.

5.1.2. Transonic test. The second comparison was performed for a transonic case (Ma = 0.55 at the inlet). Figure 9 shows an estimated error as a function of the stepsize h.

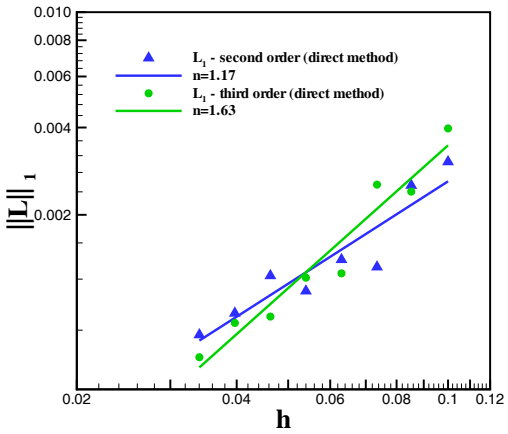

FIG. 9. Estimated $\|L\|_1$ error for transonic flow in the channel.

For transonic flow, the 3rd order method still gives better results than its 2nd order counterpart. However, this improvement of accuracy is largely obtained by reducing spurious entropy production on the wall. In the transonic case the third-order method provides thinner shock-waves (as judged by the entropy distribution – Fig. 10).

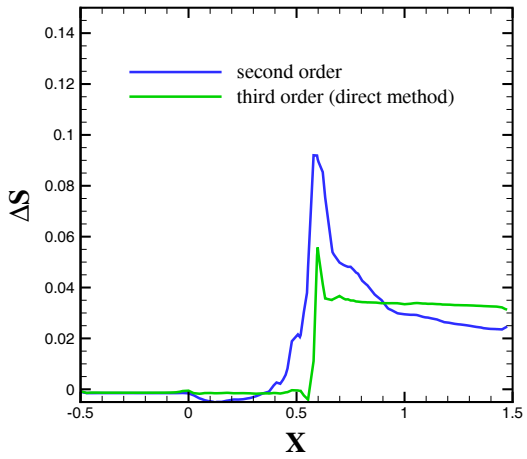

FIG. 10. Entropy distribution at the lower wall of the channel for the transonic case with Ma=0.55 at the inlet.

The entropy is calculated here by the following equation:

$$\Delta S \sim \ln \frac{p}{p_\infty} - \ln \left(\frac{\rho}{\rho_\infty} \right)^\gamma . \tag{5.2}$$

To suppress oscillation, the full WENO method was used while the gradient was evaluated using the direct method.

5.2. Onera M6 Wing

The next testcase used for verification of the third-order method is the flow past M6 ONERA wing with Mach number at infinity equal 0.84. For such a flow, two oblique shock waves merge near the tip of the wing on the upper surface (see Fig. 11).

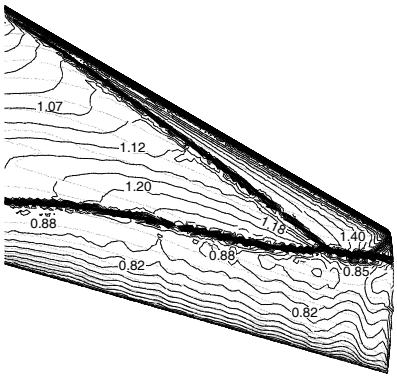

FIG. 11. Pressure coefficient distribution on the ONERA M6 wing obtained by the third-order WENO method (Ma = 0.84, $\alpha = 3.04$).

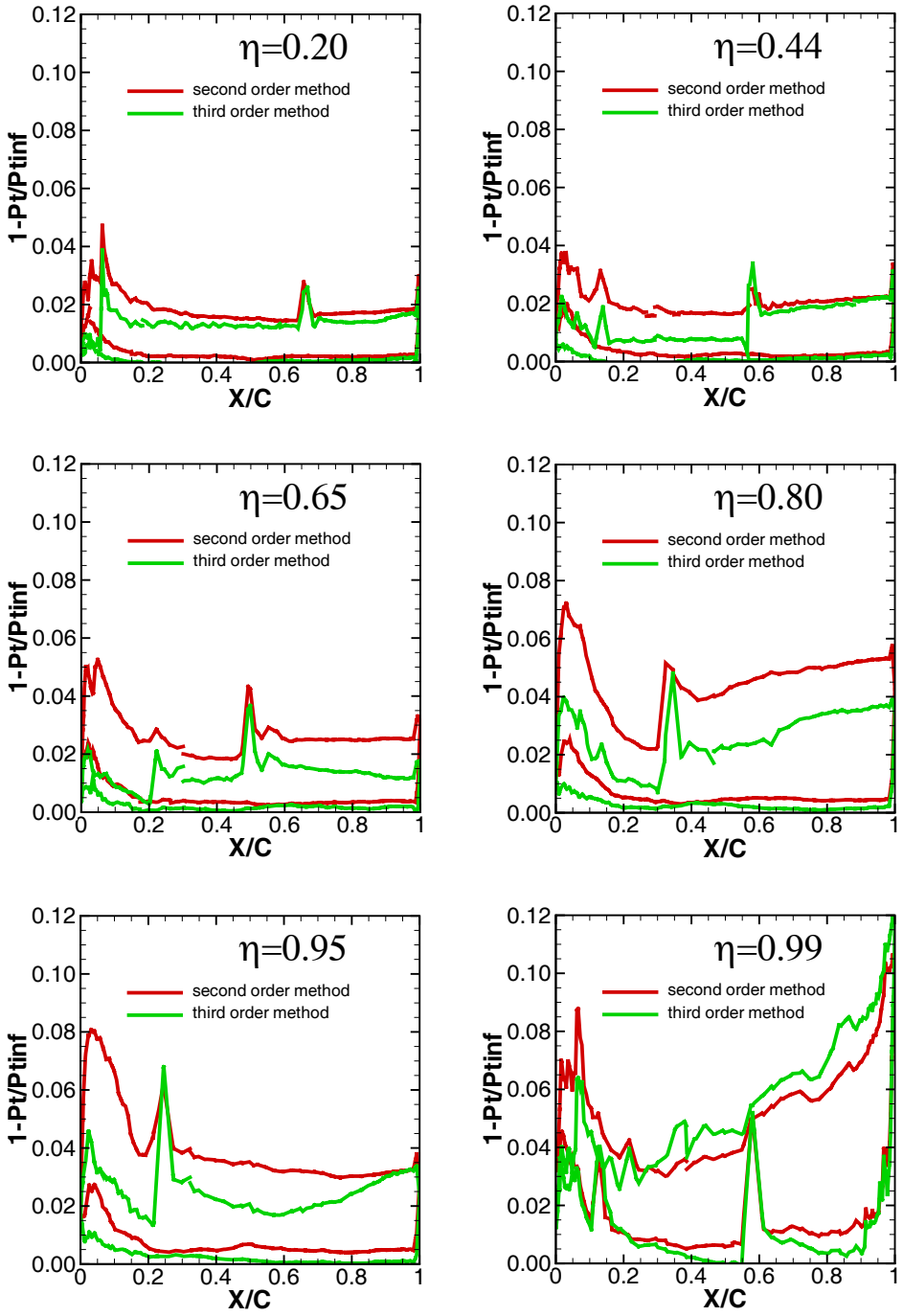

FIG. 12. Total pressure loss for different sections of M6 ONERA wing (η denotes the relative position of the cross-section), Ma = 0.84, α=3.04.

Additional results obtained by the second-order FV scheme, were used as the reference for quantitative comparison. All calculations were performed on the same grid which consisted of 316275 nodes, 1940182 cells, 2289199 edges and 3913107 faces. The pressure distribution obtained by both methods was very similar, the difference becomes visible for the total pressure loss.

Figure 12 presents total pressure loss at different sections of the wing. Total pressure loss coefficient was defined as

$$q = 1 - \frac{p_t}{p_{t\infty}}, \tag{5.3}$$

where p_t and $p_{t\infty}$ denote total pressure at a given point and at infinity, respectively. This coefficient is related to generation of spurious (numerical) entropy. Therefore lower value of this coefficient corresponds to overall higher quality simulation results.

As can be seen in Fig. 12, the third-order method generates significantly smaller amount of spurious entropy in all sections. This should improve the accuracy with which the drag coefficient is calculated (the error of the drag coefficient is directly related to the amount of spurious entropy production).

6. Computational cost

Only limited number of comparisons were made with respect to relative increase of cost between the second and third-order methods. It was estimated however that the cost of single iteration is doubled in the third-order method. Surprisingly, however, the number of nonlinear iterations was roughly equal in both approaches. This might be due to the fact that in both cases, a very simple linear preconditioner was used (in the Newton procedure) [6].

7. Conclusions

The paper deals with the cell-centred Finite-Volume WENO method, which was extended to third-order accuracy for unstructured tetrahedral (triangular) meshes. The algorithm to obtain the third-order reconstruction (including second-order gradient vector and first-order Hessian matrix) was presented, based on the general least-squares approach.

In order to deal with discontinuous solutions, the nonlinear weighting (WENO type) algorithm was adapted to the present reconstruction method. The full algorithm was tested for both the subsonic and transonic flows in the 3D channel with sinusoidal bump on the lower wall and for the Onera M6 Wing.

The subsonic results (for the sinusoidal bump) prove that the presented third-order method significantly improves the accuracy of the solution in comparison

with the standard second-order WENO method. This improvement of accuracy for transonic cases is largely obtained by reducing spurious entropy production on the wall.

References

1. C. HU, CH.-W. SHU, *Weighted Essentially Non-Oscillatory Schemes on Triangular Meshes*, J. Comput. Phys., **150**, 97–127, 1999.
2. G.S. JIANG, CH.-W. SHU, *Efficient Implementation of Weighted ENO Schemes*, J. Comput. Phys., **126**, 202–228, 1996.
3. Y. LIU, CH.-W. SHU, E. TADMOR, M. ZHANG, *Non–Oscillatory Hierarchical Reconstruction for Central and Finite Volume Schemes*, Commun. Comput. Phys., **5**, 933–963, 2007.
4. Y. LIU, M. VINOKUR, *Exact Integrations of Polynomials and Symmetric Quadrature Formulas over Arbitrary Polyhedral Grids*, J. Comput. Phys., **140**, 122–147, 1998.
5. R. WIETESKA, J. MAJEWSKI, J. ROKICKI, *Investigation of WENO Schemes for 3D Unstructured Grids*, Computer–Assisted Mechanics and Engineering Science Journal, **14**, 457–470, 2007.
6. R. WIETESKA, *Higher Order WENO method in simulation of Transonic Flows* [in Polish], PhD Thesis, Warsaw, Warsaw University of Technology, 2007.
7. J. ROKICKI, J.M. FLORYAN, *Domain Decomposition and the Compact Fourth-Order Algorithm for the Navier-Stokes Equations*, J. Comput. Phys., **116**, 79–96, 1995.

Received June 3, 2008; revised version November 26, 2008.